Enabling immobilization and conversion of polysulfides through nitrogen-doped carbon nanotubes/ultrathin MoS$_2$ nanosheets core-shell architecture for lithium-sulfur batteries

Wu Yang,[abc] Wang Yang,[abc] Liubing Dong,[b] Xiaochun Gao,[b] Guoxiu Wang,*[b]

, Guangjie Shao*[ac]

[a] State Key Laboratory of Metastable Materials Science and Technology, Yanshan University, Qinhuangdao 066004, China

[b] Centre for Clean Energy Technology, School of Mathematical and Physical Sciences, Faculty of Science, University of Technology Sydney, Broadway, Sydney, NSW 2007, Australia

[c] Hebei Key Laboratory of Applied Chemistry, College of Environmental and Chemical Engineering, Yanshan University, Qinhuangdao 066004, China

---

*Corresponding author: E-mail address: shaoguangjie@ysu.edu.cn (G. Shao), guoxiu.wang@uts.edu.au (G. Wang).
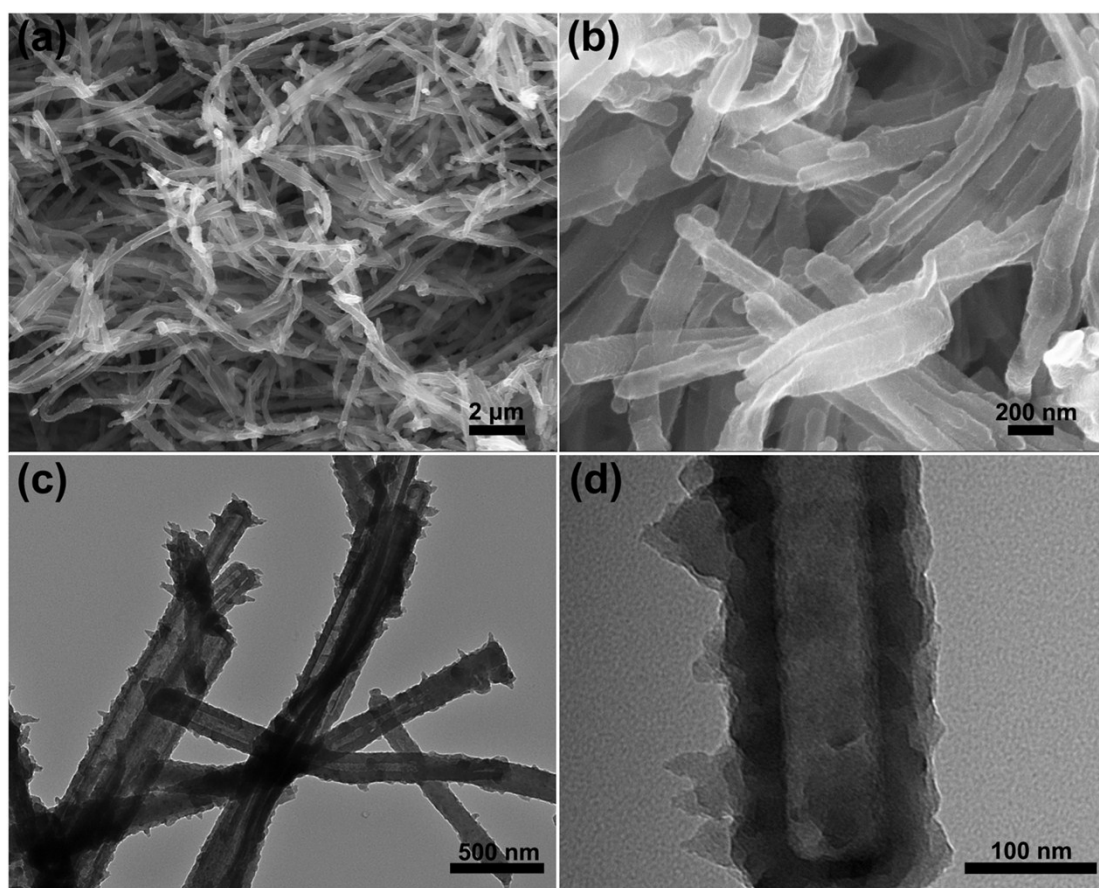
Fig. S1. SEM (a-b) and TEM (c-d) images of tubular PPy.
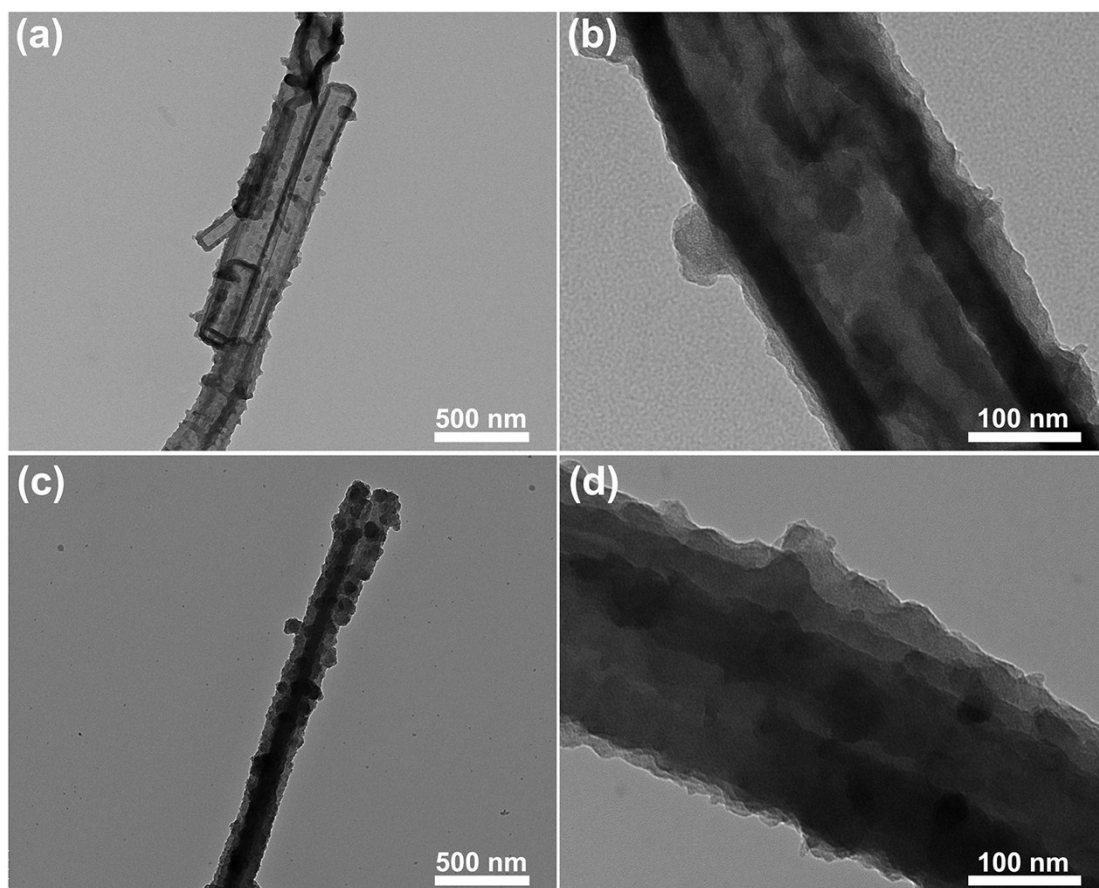
Fig. S2. TEM images of NC (a-b) and S-NC (c-d).
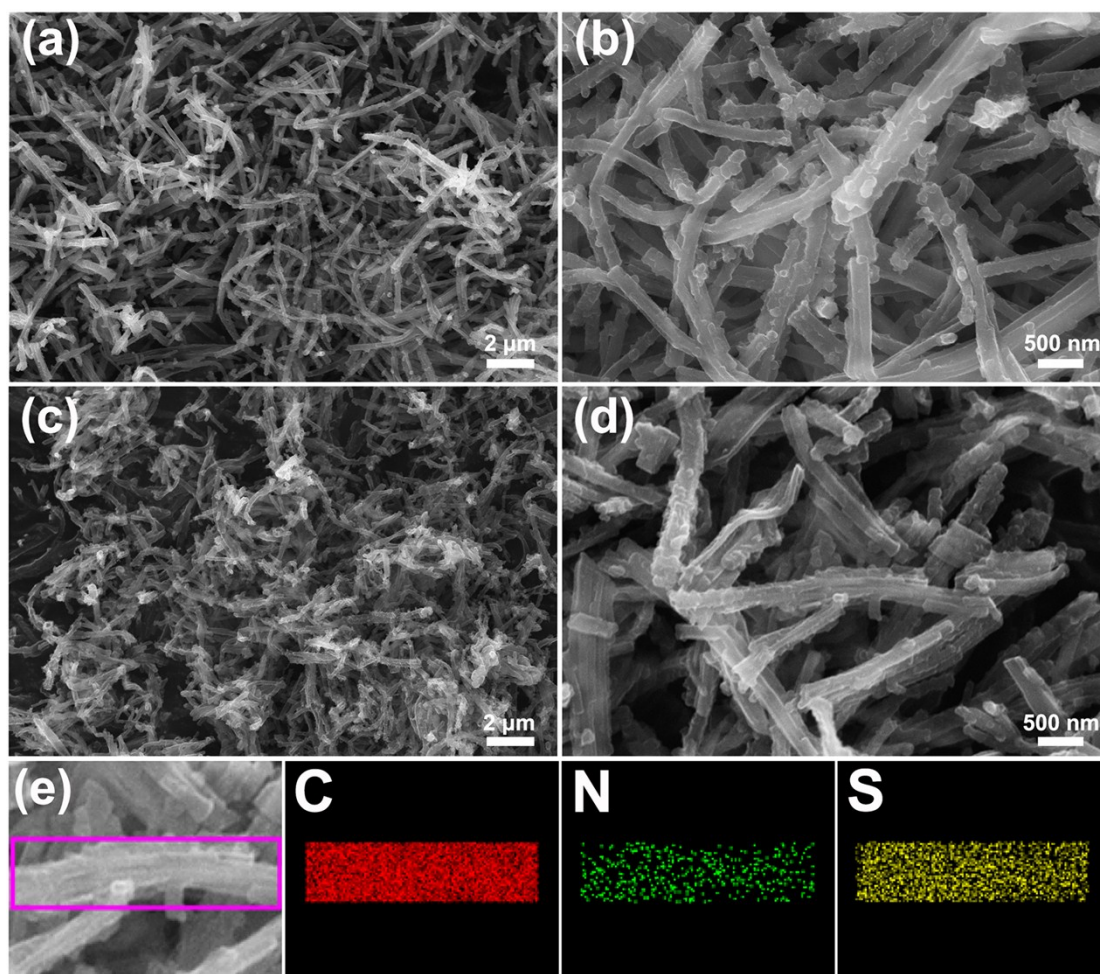
Fig. S3. SEM images of NC (a-b) and S-NC (c-d); High-magnification SEM image of S-NC and the corresponding EDS elemental mapping images of C, N, and S (e).
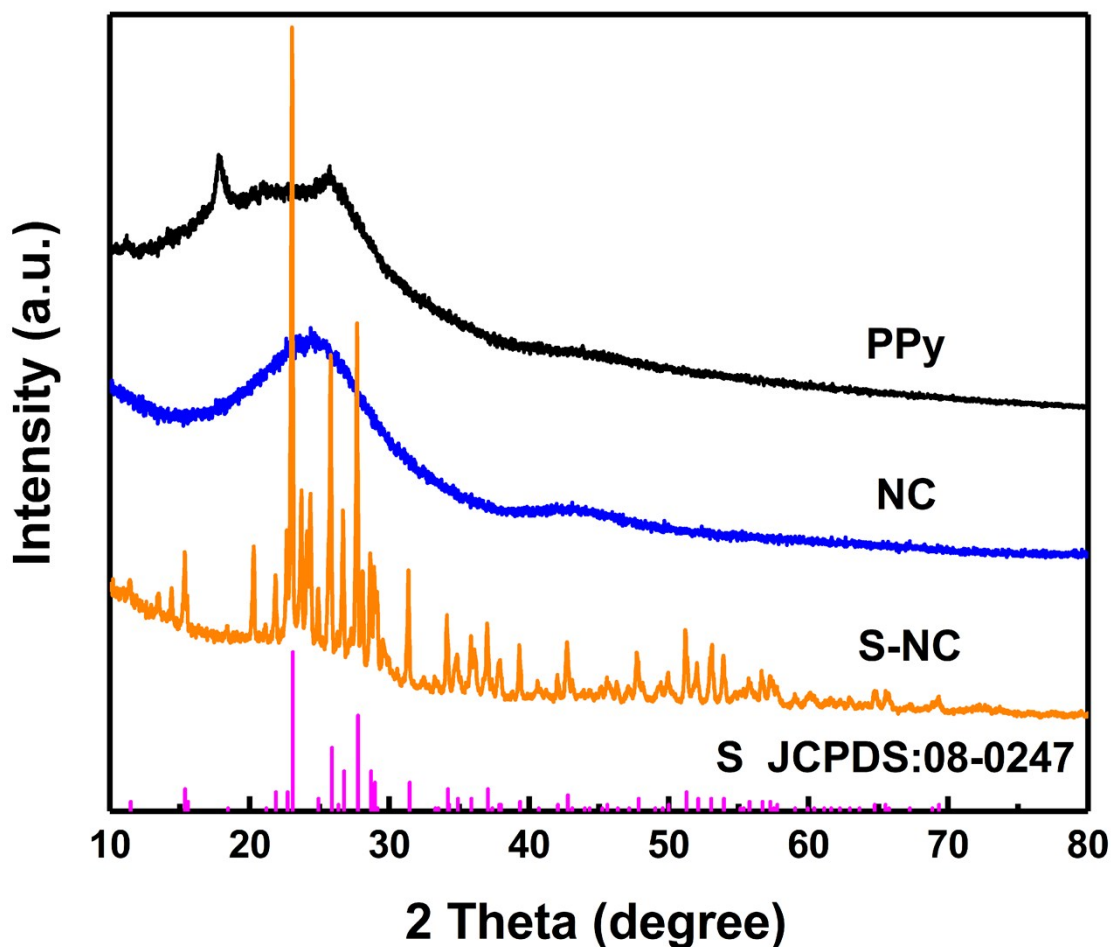
Fig. S4. XRD patterns of PPy, NC, and S-NC. Clearly, PPy has a broad and weak diffraction peak excepting two sharp diffraction peaks centered at 18° and 26°, indicating an amorphous structure and good electrical conductivity. After annealing, a broad diffraction peak centered at 24° and an inconspicuous peak centered at 43° of XRD patterns of NC were observed, corresponding to the periodically arranged (002) and (100) planes of the graphitic carbon. After sulfur impregnation, the sharp diffraction peaks centered at 23.4^o and 28.0^o match well with the (222) and (040) reflections of the orthorhombic phase sulfur (JCPDS No. 08-0247), implying that sulfur have successfully encapsulated into the internal cavity and surface of NC.
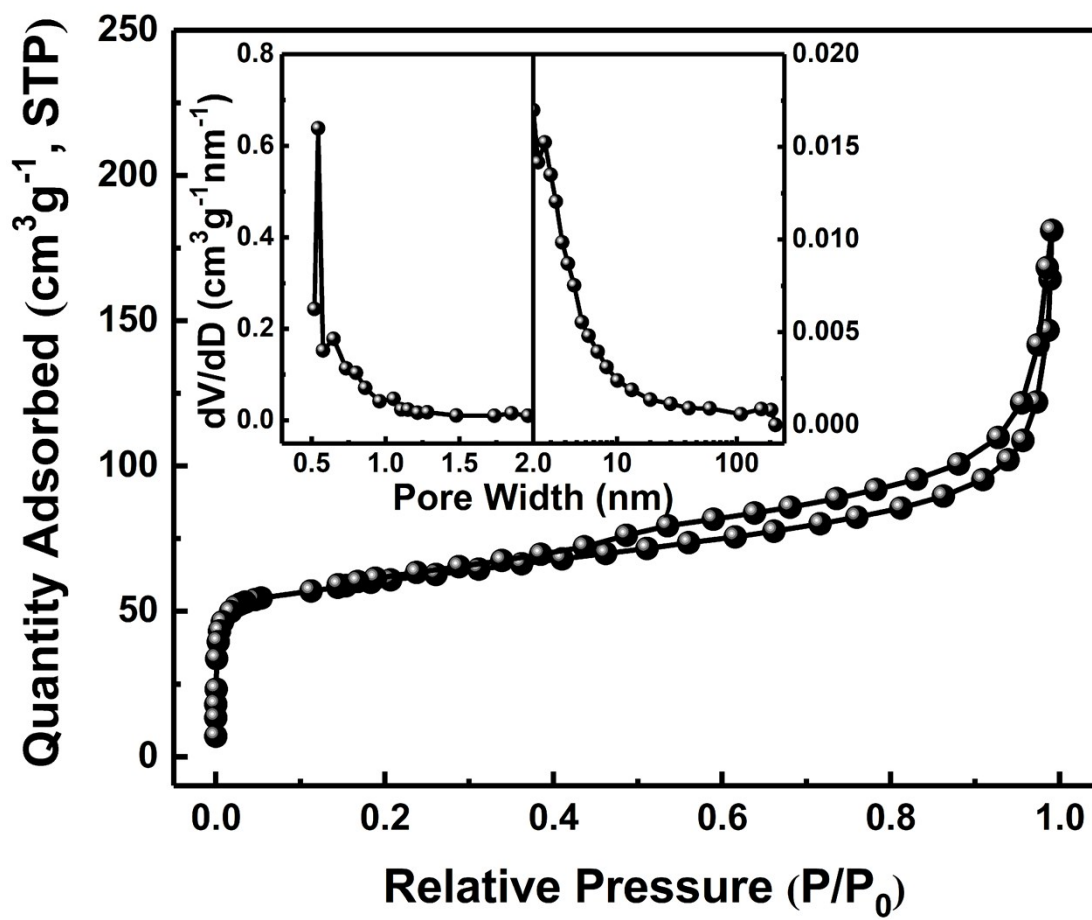
Fig. S5. Nitrogen adsorption-desorption isotherm of NC, and the inset shows the corresponding pore-size distribution.
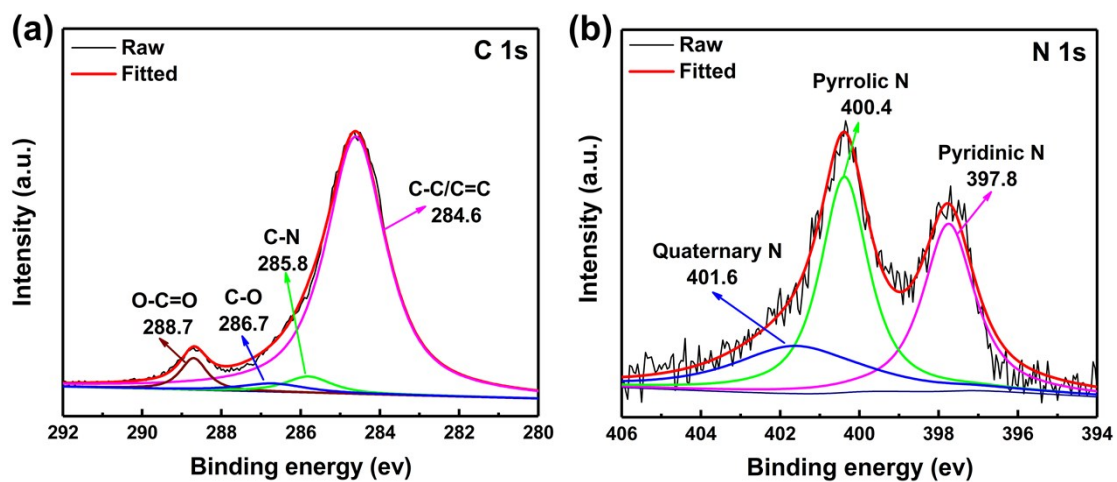
Fig. S6. C 1s (a) and N 1s (b) XPS spectra of NC.
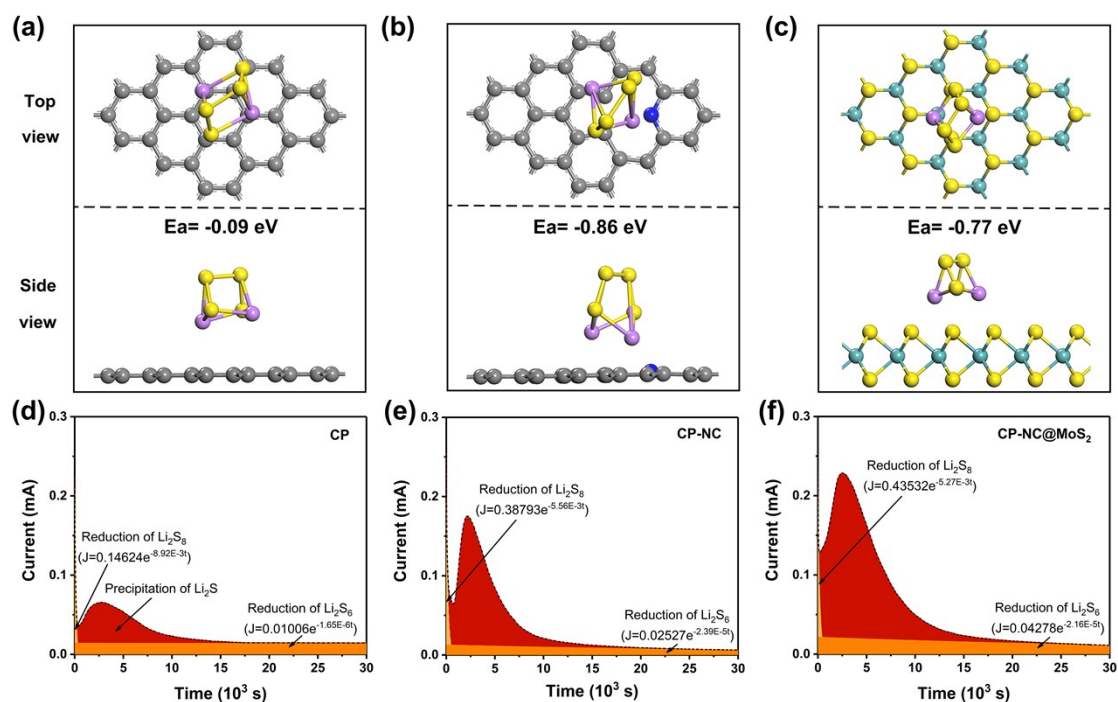
Fig. S7. Optimized geometries of Li_2S_4 on (a) carbon matrix, (b) NC, and (c) MoS_2 (001) surfaces; Fitting of current vs. time curve for potentiostatic discharge at 2.05 V on different surfaces: (d) CP, (e) CP-NC, and (f) CP-NC@MoS_2. The nucleation/growth rates of Li_2S on various surfaces were fitted according to Faraday's low, and the mathematical model is derived from Chiang and co-workers' previous work. Similarly, the potentiostatic discharge curve at 2.06 V was well fit by using the integration of two exponentially decaying curves, representing the reduction of Li_2S_8 and Li_2S_6, respectively. When an overpotential of 0.01 V was applied, Li_2S nucleated, giving rise to extra contribution to the overall current. The capacity from Li_2S formation was obtained by subtracting the capacity of Li_2S_8/Li_2S_6 reductions from overall capacities during the potentiostatic discharge curve. All the fitting results and parameters were listed in Fig. S7.
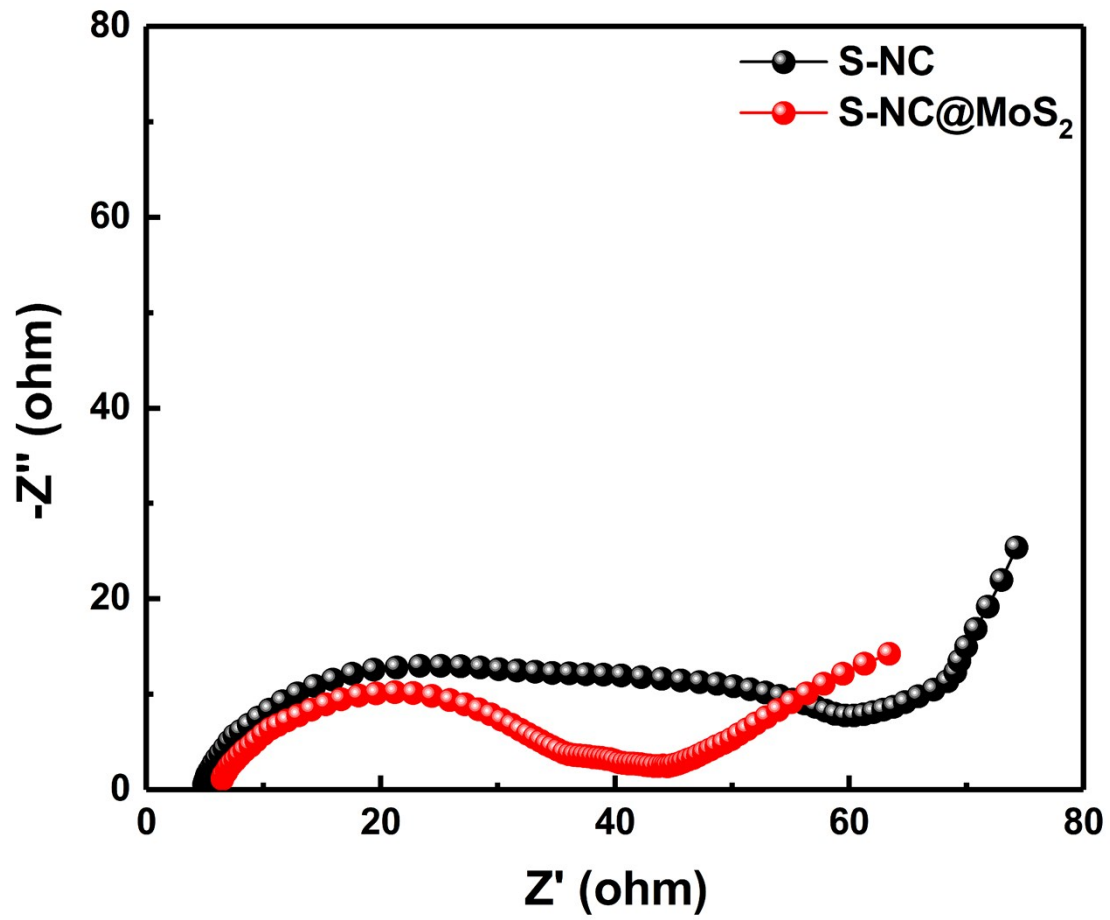
Fig. S8. Nyquist plots of S-NC@MoS$_2$ and S-NC cathodes before cycling.
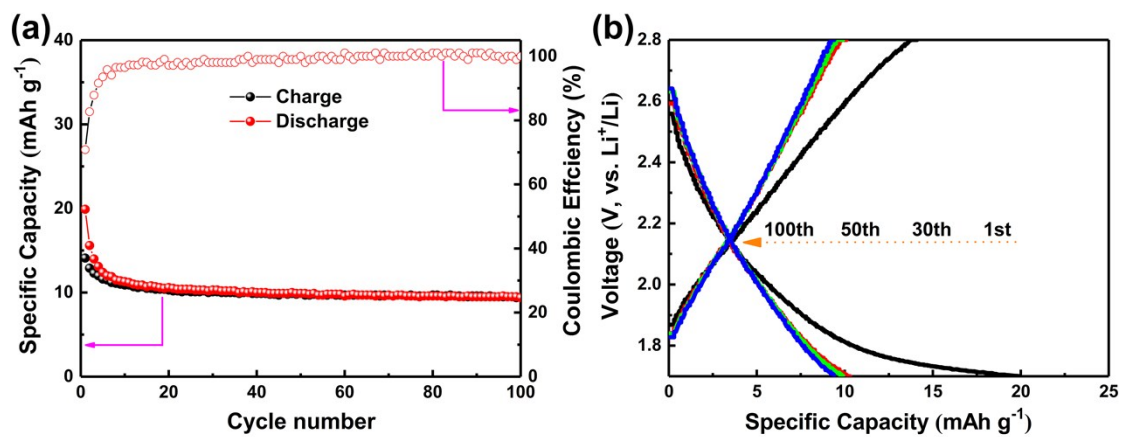
Fig. S9. Cycling performance (a) and charge/discharge profiles (b) of NC@MoS$_2$ electrode at 0.1 C.
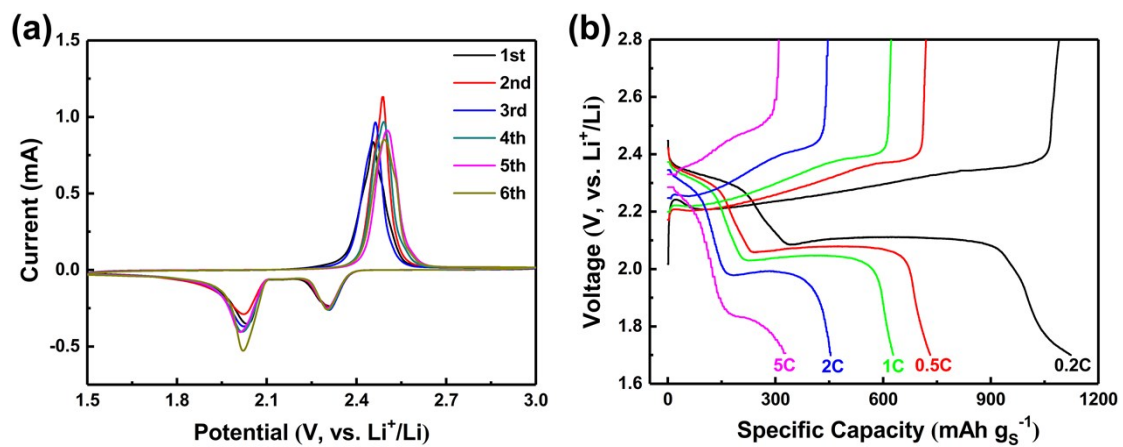
Fig. S10. CV curves of S-NC cathode (a); Charge/discharge profiles of S-NC cathode at various current densities between 0.2-5.0 C (b).
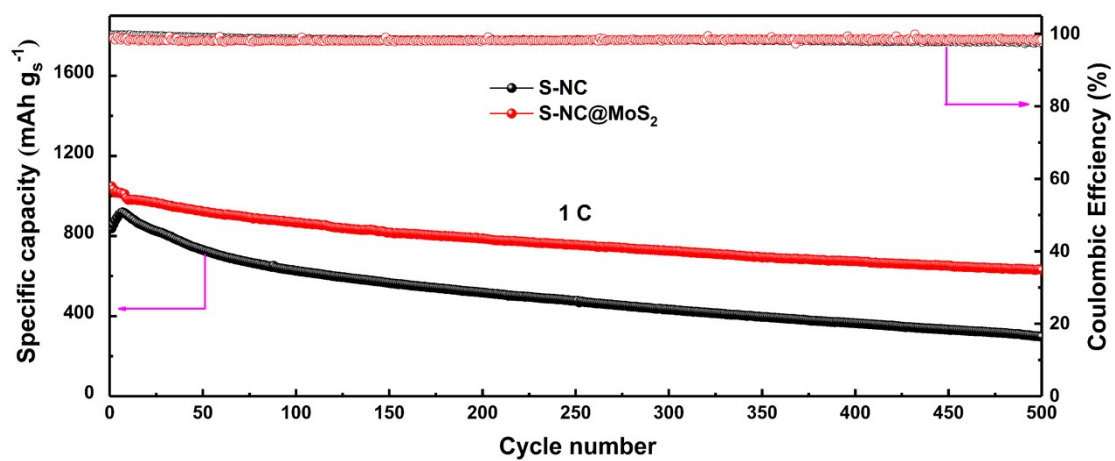
Fig. S11. Cycling performances and the corresponding Coulombic efficiencies of S-NC@MoS$_2$ and S-NC cathodes at 1 C.

Table S1. Electric conductivity of NC, MoS_2 and $NC@MoS_2$ measured at 7 MPa.

Samples	NC	MoS_2	$NC@MoS_2$
Electric conductivity (S cm^{-1})	1.23	0.05	0.56

Table S2. BET surface area, porosity parameters and chemical composition of NC and $NC@MoS_2$.

Sample	S_{BET} (m^2 g^{-1})	S_{meso} (m^2 g^{-1})	V_t (cm^3 g^{-1})	D_p (nm)	XPS (at.%)			
					C	N	Mo	S
NC	248	66	0.28	4.89	85.21	5.24	-	-
$NC@MoS_2$	29	23	0.23	42.6	79.31	5.11	12.46	3.13

S_{BET}- BET surface area, S_{meso} - BJH Adsorption cumulative surface area, V_t - total pore volume, d_p -Total adsorption average pore width.